Navigation in Difficult Environments: Multi-Sensor Fusion Techniques

Dr. Andrey Soloviev
Research and Engineering Education Facility
University of Florida
1350 N. Poquito Road
Shalimar, Florida 32579-1163
USA

Dr. Mikel M. Miller
Munitions Directorate
Air Force Research Laboratory
101 West Eglin Blvd, Bldg. 13, Ste 268
Eglin AFB, Florida 32542-6810
USA

ABSTRACT

This paper focuses on multi-sensor fusion for navigation in difficult environments where none of the existing navigation technologies can satisfy requirements for accurate and reliable navigation if used in a stand-alone mode. A generic multi-sensor fusion approach is presented. This approach builds the navigation mechanization around a self-contained inertial navigator, which is used as a core sensor. Other sensors generally derive navigation-related measurements from external signals, such as Global Navigation Satellite System (GNSS) signals and signals of opportunity (SOOP), or external observations, for example, features extracted from images of laser scanners and video cameras. Depending on a specific navigation mission, these measurements may or may not be available. Therefore, externally-dependent sources of navigation information (including GNSS, SOOP, laser scanners, video cameras, pseudolites, Doppler radars, etc.) are treated as secondary sensors. When available, measurements of a secondary sensor or sensors are utilized to reduce drift in inertial navigation outputs. Inertial data are applied to improve the robustness of secondary sensors' signal processing. Applications of the multi-sensor fusion approach are illustrated in details for two case studies: 1) integration of Global Positioning System (GPS), laser scanner and inertial navigation; and, 2) fusion of laser scanner, video camera, and inertial measurements. Experimental and simulation results are presented to illustrate performance of multi-sensor fusion algorithms.

1.0 MOTIVATION

Many existing and perspective applications of navigation systems would benefit notably from the ability to navigate accurately and reliably in difficult environments. Examples of difficult navigation scenarios include urban canyons, indoor applications, radio-frequency (RF) interference and jamming environments. In addition, different segments of a mission path can impose significantly different requirements on the navigation sensing technology and data processing algorithms. To exemplify, Figure 1 shows a mission scenario of an autonomous aerial vehicle (UAV).

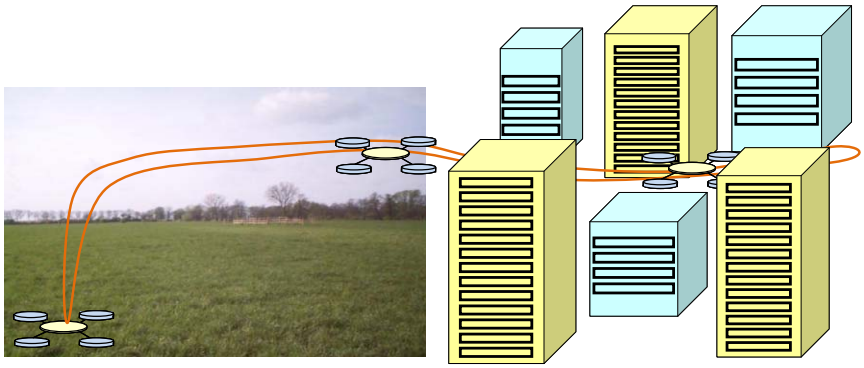

Figure 1: UAV mission example.

For this example, the UAV is deployed in an open field; next, the vehicle enters an urban canyon to perform tasks such as surveillance and reconnaissance; and, finally, it returns to the deployment point. To enable operation of the UAV at any point on the flight path, a precision navigation, attitude, and time capability on-board the vehicle is required. Global Navigation Satellite System (GNSS) generally provides satisfactory performance in open fields and suburban areas, but has fragmented availability in urban environments due to satellite blockages by buildings and other obstacles. Feature-based navigation techniques demonstrate a promising potential in dense urban areas where enough navigation-related features can be extracted from images of digital cameras or laser scanners. However, the feature availability can be limited in relatively open areas. A self-contained inertial navigation system (INS) can provide navigation solution at any environment; however, the solution accuracy drifts over time. In a stand-alone mode, none of the existing navigation technologies has a potential to satisfy the requirements for the navigation accuracy, continuity and availability over the entire duration of the UAV flight. Therefore, multi-sensor fusion techniques are pursued. In other words, to be able to navigate at any environment at any time, it is beneficial to utilize any potential source of navigation related information.

Example applications that involve navigation in difficult environments include but are not limited to navigation, guidance and control of autonomous ground vehicle (UGV) and autonomous aerial vehicle (UAV), as well as teams of UGVs and UAVs for urban surveillance and reconnaissance tasks; geographical information system (GIS) data collection for mapping applications on open highways and dense urban environments; indoor search and rescue applications; monitoring of urban infrastructure for situational awareness; and, precise automotive applications such as automated lane keeping. Meter-level to decimeter-level reliable positioning capabilities are generally needed for these application examples. As stated previously, none of the existing navigation technologies can currently satisfy these requirements or has a potential to provide these capabilities in a stand-alone mode.

This paper discusses multi-sensor fusion approaches for navigation in difficult environments. A generic concept of the multi-sensor fusion is first presented. Next, the paper exemplifies applications of the generic multi-sensor fusion concept for the development of specific multi-sensor mechanizations. Specifically, integrated Global Positioning System (GPS)/laser scanner/INS and laser scanner/video camera/INS mechanizations are considered.

2.0 MULTI-SENSOR FUSION APPROACH

The generic concept of the multi-sensor navigation utilizes a self-contained inertial navigator as a core navigation sensor. The INS does not rely on any type of external information and as a result can operate in any

environment. However, inertial navigation solution drifts over time [1]. To mitigate INS drift, this core sensor is augmented by reference navigation data sources (such as, for example, GPS or a laser scanner). Reference data sources generally rely on external observations or signals that may or may not be available. Therefore, these sources are treated as secondary sensors. When available, secondary sensors' measurements are applied to reduce the drift in inertial navigation outputs. Inertial data are used to bridge over reference sensor outages. In addition, inertial data can be applied to improve the robustness of reference sensor signal processing: for instance, to significantly increase the GPS signal integration interval in order to enable processing of very weak GPS signals and to reduce the susceptibility of GPS to radio-frequency interference [2]. Figure 2 illustrates the multi-sensor fusion approach.

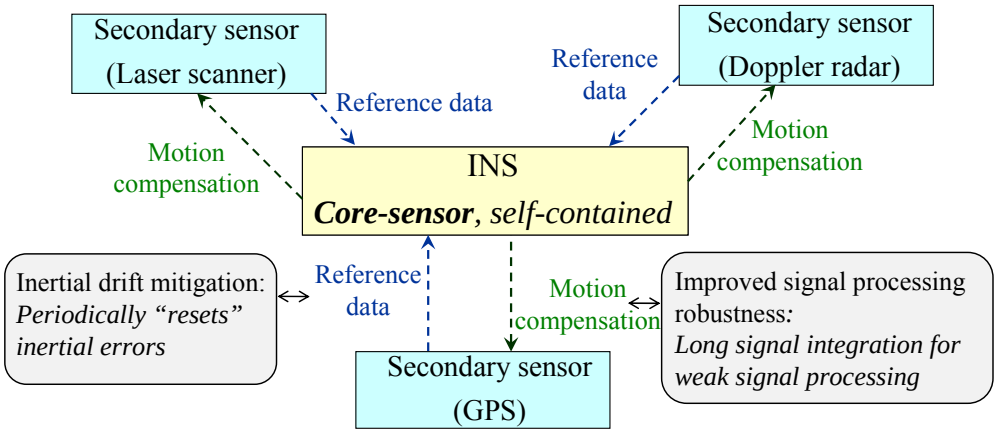

Figure 2: Generic multi-sensor fusion approach.

Figure 3 provides a more detailed illustration of the interaction between the INS and a secondary navigation sensor.

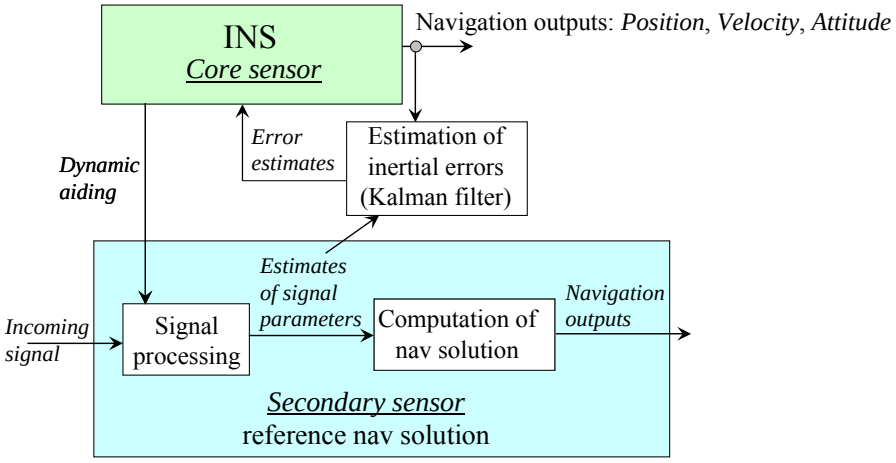

Figure 3: Data fusion between the INS and a secondary navigation sensor.

The secondary sensor generally includes a signal processing part and a navigation solution part. The signal processing part receives navigation-related signals and measures their parameters. For example, GPS receiver

tracking loops [3] or open-loop batch estimators [4] measure parameters (pseudoranges, Doppler frequency shift, and carrier phase) of the received GPS signals. Another example is a laser scanner time-of-flight measurement that is directly related to the distance between the scanner and a reflecting object. Measurements of signal parameters are then applied to compute the navigation solution. For example, GPS pseudoranges are used to compute the GPS receiver position [3], changes in distances to reflecting stationary objects are exploited to compute the change in the position of the laser scanner [5]. Note that the navigation solution can only be computed if a sufficient number of signal measurements is made. For example, at least four pseudorange measurements must be available to compute the GPS-based position; at least two lines must be extracted from an image of a two-dimensional (2D) laser scanner to compute a 2D laser position [5].

The multi-sensor fusion architecture above applies secondary sensor's signal measurements to estimate drifts in inertial navigation outputs. This approach is generally referred to as tight coupling. The use of signal measurements for the INS drift re-calibration is more beneficial as compared to the use of the secondary sensor's navigation solution (this form of sensor fusion is referred to as loose coupling). As opposed to loose coupling, tight coupling still allows for the INS drift mitigation even for those cases where insufficient number of signal measurements is available and the complete navigation solution cannot be derived.

The estimation of the INS drift terms is performed using the mechanism of a complementary Kalman filter. The idea is that a signal parameter can be generally represented as a function of position, velocity and attitude. This function is computed based on INS navigation outputs and then compared to the actual signal measurement. A discrepancy between the INS-based signal prediction and the signal measurement is used by the complementary Kalman filter mechanization to estimate INS drift terms. A generic Kalman filter measurement observable $\mathbf{y}$ is formulated as follows:

$$\mathbf{y} = \rho(\mathbf{R}_{INS}, \mathbf{V}_{INS}, \boldsymbol{\alpha}_{INS}) - \tilde{\rho} \tag{1}$$

where:

$\mathbf{R}_{INS}$ is the INS position vector;

$\mathbf{V}_{INS}$ is the INS velocity vector;

$\boldsymbol{\alpha}_{INS}$ is the INS attitude (that can be represented as a direction cosine matrix, rotation vector, rotation quaternion, or Euler angles [1]);

$\rho(\mathbf{R}_{INS}, \mathbf{V}_{INS}, \boldsymbol{\alpha}_{INS})$ is the signal value predicted based on the inertial output; and,

$\tilde{\rho}$ is the actual signal measurement.

The signal measurement herein is denoted by ρ since the tight coupling approach was first applied to the GPS/INS integration case in order to fuse GPS pseudorange measurements and integrated Doppler range measurements with inertial data [6]. For this reason, the INS calibration in the signal measurements' domain is also often referred to as the range-domain data fusion. Obviously, the formulation above is not limited to the GPS/INS integration case and is applicable to any type of navigation-related signal measurements. It is important to mention that video measurements serve as an exclusion for this general rule of the observation formulation. For a vision-based case where the distance to a navigation-related feature is unknown and cannot be measured (for example, a monocular camera case without any prior feature information), image features are related to navigation parameters not in the form of a non-linear function, but rather in the form of a non-linear motion constraint. This constraint is formulated as $f(\mathbf{R}, \boldsymbol{\alpha}, \mathbf{m}, \rho) = 0$, where $\mathbf{m}$ represents feature homogeneous coordinates (i.e., Cartesian coordinates scaled by the image depth) and ρ is the distance to the feature. In this case, non-linear motion constrains and inertial data are used to formulate Kalman filter

observables: i.e., $f(\mathbf{R}_{INS},\boldsymbol{\alpha}_{INS},\tilde{\mathbf{m}},\rho)=0$, where $\tilde{\mathbf{m}}$ denotes homogeneous feature coordinates that are extracted from video images.

To implement a complementary Kalman filter, equation (1) is linearized as using a Taylor series expension:

$$\begin{aligned} \not{y} &= \rho(\mathbf{R}_{INS},\mathbf{V}_{INS},\boldsymbol{\alpha}_{INS}) - \tilde{\rho} \\ &\approx \rho + \frac{\partial\rho}{\partial\mathbf{R}_{INS}}\delta\mathbf{R}_{INS} + \frac{\partial\rho}{\partial\mathbf{V}_{INS}}\delta\mathbf{R}_{INS} + \frac{\partial\rho}{\partial\boldsymbol{\alpha}_{INS}}\delta\boldsymbol{\alpha}_{INS} - (\rho - n_\rho) \\ &= \frac{\partial\rho}{\partial\mathbf{R}_{INS}}\delta\mathbf{R}_{INS} + \frac{\partial\rho}{\partial\mathbf{V}_{INS}}\delta\mathbf{R}_{INS} + \frac{\partial\rho}{\partial\boldsymbol{\alpha}_{INS}}\delta\boldsymbol{\alpha}_{INS} - n_\rho \end{aligned} \quad (2)$$

where:

ρ is the true value of the signal parameter;

n_ρ is the measurement noise; and

$\delta\mathbf{R}_{INS}$, $\delta\mathbf{V}_{INS}$, and $\delta\boldsymbol{\alpha}_{INS}$ are the INS position, velocity and attitude errors, respectively.

Non-linear motion constraints are linearized for the case of video measurements. These linearized formulations are then utilized by standard Kalman filter routines (i.e., prediction, estimation and covariance updates) to estimate INS error states.

For those cases where multiple measurements are available from secondary navigation sensors, the measurement observation vector is expressed as follows:

$$\begin{aligned} &\{\not{y}_l^{(i)}\} = \rho_l^{(i)}(\mathbf{R}_{INS},\mathbf{V}_{INS},\alpha_{INS}) - \tilde{\rho}_l^{(i)} \\ &l = 1,...,L \\ &i = 1,...,I \end{aligned} \quad (3)$$

In (3), l is the reference sensor index and i is the measurement index for a particular reference sensor. For example, reference sensors can include GPS, laser scanner and Doppler radar with corresponding indexes 1, 2, and 3. In this case, $\not{y}_2^{(5)}$ represents a 5th measurement observable for laser scanner measurements. Specific formulations of Kalman filter measurement observations are exemplified in Section 3 for cases of GPS, laser scanner and vision reference sensors.

As mentioned previously, while the secondary sensors' measurements are used to improve the inertial accuracy, the INS data can be applied to improve the robustness of the secondary sensor's signal processing. For example, inertial data can be used for robust matching of features between different images of a video camera or a laser scanner. Another example is the use of inertial aiding for GPS signal integration in order to enable tracking of signals that are attenuated by buildings [7].

Secondary navigation sensors that can be applied for the multi-sensor fusion with the INS include:

GNSS and partial GNSS: GPS and GNSS signal measurements can be efficiently integrated with inertial data in open areas and also in difficult GPS signal environments (such as urban areas) where limited GNSS signals may still be available [7], [8].

Feature-based navigation sensors: Examples include image-aided inertial navigation [9] and ladar-aided inertial navigation [5].

Beacon-based navigation (including pseudolites): If the GPS signal is not adequate for navigation in a particular environment, it is possible to transmit an additional signal or signals that are specifically designed for navigation purposes. If the transmitted signals are similar to GPS signals, then such beacon transmitters are usually called "pseudolites." Examples of beacon-based navigation systems for indoor navigation can be found in [10] and [11].

Signals of opportunity (SoOP). Signals of opportunity, as defined in this paper, are radio frequency (RF) signals that are not intended for navigation. Examples from previous research include digital television [12], analog television[13], and AM radio [14], [15].

The remainder of this paper illustrates application of the generic multi-sensor fusion approach described above GPS/laser/inertial and vision/laser/inertial integrated mechanizations.

3.0 EXAMPLE MULTI-SENSOR FUSION MECHANIZATIONS

3.1 GPS/Laser Scanner/Inertial

Feature-based navigation techniques represent a viable option for navigation in difficult GPS environments. For example, the integrated laser scanner/INS solution was demonstrated to provide sub-meter accurate navigation for dense urban environments where multiple lines can be extracted from scan images [5]. However, the feature-based navigation approach clearly has its limitations. Relatively open streets represent challenging conditions for the line-based navigation due to limited line availability. To illustrate, Figure 4 shows a scan image recorded on a relatively open street. For this example, only one line is extracted from the image and the system must augment its position computations by the INS coasting option.

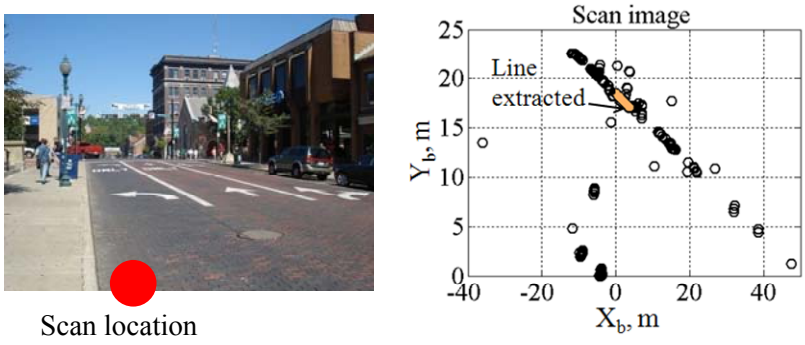

Figure 4: Example of the laser scan image taken on a relatively open street: only one line is extracted from the image, which is insufficient to compute the position solution.

In addition, even in dense urban canyons, line geometry observed in scan images can be insufficient to support complete observability of the navigation states.

Figure 5 illustrates the case where lines in the scan image are created by two nearly parallel building walls. In this case, lines extracted from laser scans are nearly collinear. This line geometry allows for the estimation of the cross-track position component only: i.e., the vehicle motion component in the direction perpendicular to

the walls can be estimated, while the along-track (parallel to the walls) motion component is unobservable and INS coasting has to be used to compute vehicle displacement in this direction.

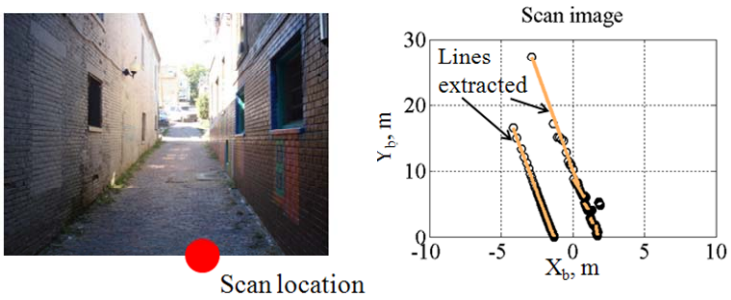

Figure 5: Example of the laser scan in an urban canyon: nearly collinear lines are extracted, which limits the observability of position states.

The use of GPS can efficiently augment the feature-based navigation approach. Relatively open streets (see, for example, Figure 4) generally provide enough open sky visibility to track a number of GPS satellite signals that is sufficient for navigation computations. In dense urban canyons where only limited feature geometry is available (see, for example, Figure 5), a reduced number of satellite signals can be still trackable through limited portions of an open sky. Combining line measurements with these additional GPS measurements can complete the observability of navigation states. To exemplify, the availability of high-elevation satellites that have line-of-sight azimuth angles aligned with the direction of an urban canyon shown in Figure 5 can complete the observability for the along-track position component. In this case, two satellites are required to complete the 2D position and clock solution. One satellite is sufficient for the case where a reliable estimate of the GPS receiver clock bias is available: i.e. the receiver clock bias and clock drift have been previously estimated and the clock stability figures allow for an accurate propagation of the clock state estimates from the estimation time to the current measurement epoch.

Integration of GPS, laser scanner and inertial data is discussed in the remainder of this subsection. Figure 6 illustrates the integrated system architecture.

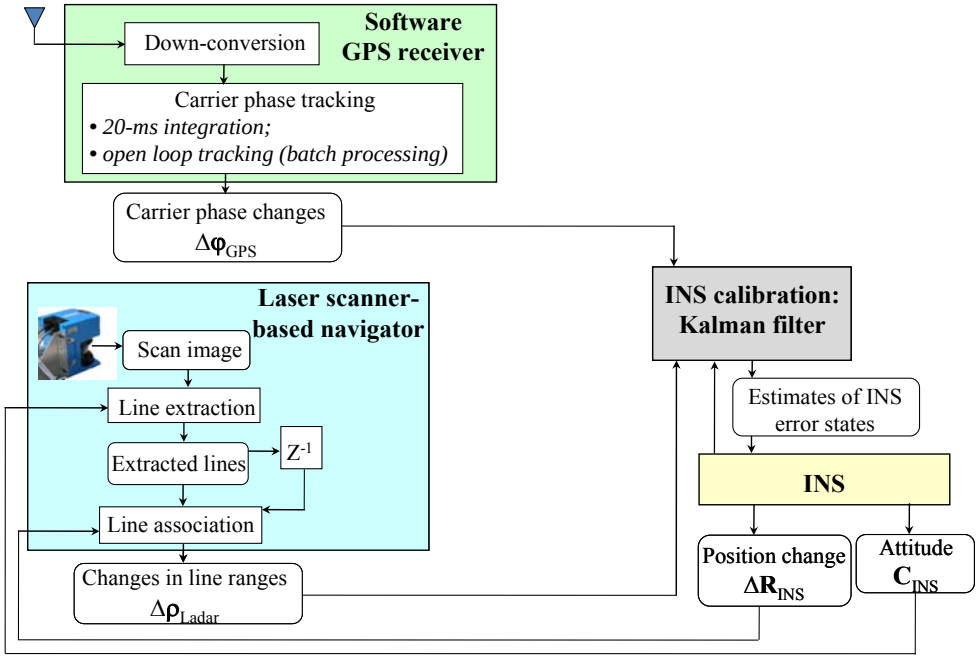

Figure 6: Integrated GPS/laser scanner/INS system architecture.

This architecture combines GPS, laser scanner, and inertial data for trajectory reconstruction, i.e. the estimation of changes in the user position (or delta position) between successive GPS and laser measurement epochs. An open loop software GPS receiver [4] is exploited for robust carrier phase tracking in difficult environments. The integrated solution utilizes INS navigation outputs to improve the solution robustness. Particularly, inertial data are applied to 1) predict feature displacements between laser scans for robust feature association between scan images, and, 2) computationally adjust a 2D scan plane for tilting of the laser scanner platform.

As shown in Figure 6, a Kalman filter is used to periodically compute estimates of inertial error states that are then applied to mitigate the drift in INS navigation outputs. Kalman filter observables are formulated in the measurement domain of GPS and laser scanner, which is, as mentioned previously, referred to as range-domain data fusion. Specifically, changes in GPS carrier phase measurements and changes in ranges to lines extracted from scan images serve as filter measurement observables. A complementary filter formulation [16] is utilized for the efficient linearization of system state relations: i.e., filter measurement observables are computed as differences between GPS (and/or laser scanner) measurement observables and INS navigation outputs transformed into the GPS (and/or laser scanner) measurement domain. In addition, a dynamic-state filtering approach [17] is exploited. In this case, the filter implements displacement error states (dynamic states) rather than absolute position error states.

GPS observables of the Kalman filter are based on carrier phase single differences (SDs) between the filter update epochs. The SD approach allows exploiting mm-level accurate carrier phase measurements for trajectory reconstruction without the need to resolve integer ambiguities. Equation (4) formulates the carrier phase SD equation [18]:

$$\Delta\tilde{\varphi}_j = \tilde{\varphi}_j(t_M) - \tilde{\varphi}_j(t_{M-1}) = \Delta r_j + \Delta\delta t_{rcvr} + \Delta errors_j + \Delta\eta_j \quad (4)$$

where:

$\Delta\tilde{\varphi}_j$ is the carrier phase SD for satellite j;

$\tilde{\varphi}_j$ is the carrier phase measurement for satellite j;

$t_M = t_0 + M \cdot \Delta t_{GPS}$ is the discrete time and Δt_{GPS} is the GPS measurement update interval;

$\Delta r_j = r_j(t_M) - r_j(t_{M-1})$ is the SD of the range r_j between the GPS antenna and satellite j;

$\Delta\delta t_{rcvr}$ is the SD of the receiver clock bias, or, equivalently, the receiver clock drift accumulated over the Δt_{GPS} interval;

the $\Delta errors_j$ term represents changes in deterministic error components of stand-alone GPS measurements and includes changes in ionospheric and tropospheric delays, changes in the satellite clock bias, and drift components of relativistic corrections; and,

$\Delta\eta_j$ is the joint noise and multipath term, which includes carrier noise and multipath.

The SD in satellite/receiver range is expressed as follows:

$$\Delta r_j = \text{SV Doppler}_j - \Delta\text{geometry}_j - \left(\mathbf{e}_j(t_M), \Delta\mathbf{R}\right) \tag{5}$$

where:

SV Doppler_j is a change in the range due to the satellite motion along the line-of-sight (LOS);

$\Delta\text{geometry}_j$ accounts for changes in the relative satellite/receiver geometry;

$\mathbf{e}_j$ is the unit vector pointed from the receiver to the satellite, this vector is generally referred to as the LOS unit vector;

$\Delta\mathbf{R}$ is the receiver position change vector for the interval $[t_{M-1}, t_M]$; and,

(,) is the vector dot product.

Carrier phase SDs are adjusted for the satellite motion terms, geometry terms, and delta error terms prior to their exploitation as Kalman filter measurement observables. For the SD adjustment, satellite motion and geometry terms are computed as follows [18]:

$$\text{SV Doppler}_j = \left(\mathbf{e}_j(t_M), \mathbf{R}_{SVj}(t_M)\right) - \left(\mathbf{e}_j(t_{M-1}), \mathbf{R}_{SVj}(t_{M-1})\right) \tag{6}$$

$$\Delta\text{geometry}_j = \left(\mathbf{e}_j(t_M) - \mathbf{e}_j(t_{M-1}), \mathbf{R}(t_{M-1})\right) \tag{7}$$

In (6) and (7):

$\mathbf{R}_{SVj}$ is the satellite position vector; and,

$\mathbf{R}$ is the receiver position vector.

For geometry compensation, the receiver position vector $\mathbf{R}$ at the previous update (t_{M-1}) is estimated based on GPS pseudorange measurements. For those cases where not enough pseudorange measurements are available, the position estimate is propagated using inertial data. Note that a sub-hundred-m level accurate position estimate is generally sufficient to support mm-level accuracy in the carrier phase SDs [18]. The satellite position $\mathbf{R}_{SVj}$ vector is computed from ephemeris data, and the LOS unit vector $\mathbf{e}_j$ is computed based on

ephemeris data and the pseudorange-based receiver position estimate. Tropospheric drift terms are compensated based on tropo models [3]. Iono delta errors are normally compensated using dual frequency measurements [3]. However, generally, iono drift terms stay at a mm/s level or less unless ionospheric scintillations are present [18]. Thus, for most operational scenarios, uncompensated iono drift does not significantly influence the accuracy of carrier phase SDs. For this reason, the system mechanization reported in this paper does not implement iono corrections.

From equation (4) and (5), carrier phase SDs that are adjusted for the satellite motion, geometry changes, and delta error terms are expressed as follows:

$$\Delta\tilde{\varphi}_j^{adj}(t_M) = -\left(\mathbf{e}_j(t_M), \Delta\mathbf{R}\right) + \Delta\delta t_{rcvr} + \Delta\eta_j \tag{8}$$

GPS observables of the Kalman filter are computed as differences between INS-based predicted values of carrier phase SDs and carrier phase SDs that are actually measured by the GPS receiver. For satellite j, this difference is formulated as:

$$u_j^{Kalman} = \Delta\tilde{\varphi}_j^{INS} - \Delta\tilde{\varphi}_j^{adj} \tag{9}$$

where:

$$\Delta\tilde{\varphi}_j^{INS} = -\left(\mathbf{e}_j(t_M), \Delta\tilde{\mathbf{R}}_{INS} + \Delta\tilde{\mathbf{C}}_b^N \cdot \mathbf{L}_{IMU}^{GPS}\right) \tag{10}$$

In (10), $\Delta\tilde{\mathbf{C}}_b^N = \tilde{\mathbf{C}}_b^N(t_M) - \tilde{\mathbf{C}}_b^N(t_{M-1})$ and $\mathbf{L}_{IMU}^{GPS}$ is the lever-arm vector between the inertial measurement unit (IMU) and GPS antenna with the lever arm vector components being resolved in the body frame. Equations (9) and (10) illustrate the specific implementation of the generic multi-sensor fusion observable, which is formulated by equation (1), for the case where GPS carrier phase measurements serve as reference measurements for the INS drift estimation.

Laser scanner observables of the Kalman filter are computed from navigation related features observed in scan images. These observations are illustrated in Figure 7.

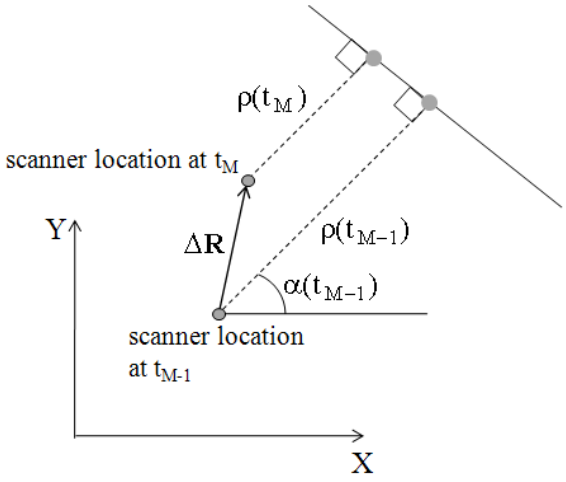

Figure 7: Laser scanner motion and observed change in line parameters.

For the laser scanner case, lines are chosen as the basis navigation feature [5]. Kalman filter observables are formulated based on changes in line parameters between consecutive scans. As illustrated in Figure 7, changes in the scanner location between scans create changes in parameters of lines observed in scan images. In Figure 7, line is represented by its normal point, where a normal point is defined as a perpendicular intersection of the line itself and the line originating from the scanner location. Line normal points are characterized by their polar parameters: range ρ and angle α. From the geometry shown in Figure 7, position change is related to the line range change as follows [5]:

$$\Delta\tilde{\rho}_k = \tilde{\rho}_k(t_M) - \tilde{\rho}_k(t_{M-1}) = -\Delta R_X \cos\left(\alpha_k(t_{M-1})\right) - \Delta R_Y \sin\left(\alpha_k(t_{M-1})\right) + \Delta\varepsilon_k \tag{11}$$

where:

$\Delta\tilde{\rho}_k$ is the line range change for line k;

$\tilde{\rho}_k$ is the line range estimated by a line extraction procedure (e.g., using a modified iterative split and merge line extraction algorithm described in reference [19]);

ΔR_X and ΔR_Y are position change components;

α_k is the line angle; and,

$\Delta\varepsilon_k$ is the noise in estimated line delta range that is due to line extraction errors; these errors generally comprise of laser measurement noise and a texture of a scanned surface.

Note that equation (11) operates with line parameters that are transformed into the horizontal plane using the laser tilt compensation procedure described in [5]. Lines are observed at the laser scanner body frame. This frame can be tilted due to non-zero pitch and roll angles of the scanner platform. The tilt compensation procedure exploits INS attitude outputs to project lines observed in the scanner body-frame onto a horizontal plane of the navigation frame in order to mitigate the influence of laser tilt angles on the navigation solution accuracy. Thus, equation (11) relates changes in line parameters with changes in position vector components that are resolved in the axes of the navigation frame. For the system implementation considered in this paper, navigation is performed at the East-North-Up (ENU) frame. Laser scanner body-frame and body-frame of the inertial measurement unit (IMU) are computationally aligned to the axes of the navigation frame during the system initialization stage. IMU body-frame is physically aligned with the laser body-frame and misalignment errors are calibrated during the system initialization.

Below, equation (11) is reformulated in a vector form:

$$\Delta\tilde{\rho}_k = -\left(\mathbf{n}_k(t_M), \Delta\mathbf{R}\right) + \Delta\varepsilon_k \tag{12}$$

where:

$$\mathbf{n}_k(t_{M-1}) = \left[\cos\left(\alpha_k(t_{M-1})\right) \quad \sin\left(\alpha_k(t_{M-1})\right) \quad 0\right]^T \tag{13}$$

A laser scanner observable of the Kalman filter is computed as a difference between line delta range predicted based on inertial data and a line delta range extracted from scanner measurements. For line p, this is formalized as follows:

$$v_k^{\text{Kalman}} = \Delta\tilde{\rho}_k^{\text{INS}} - \Delta\tilde{\rho}_k \tag{14}$$

where:

$$\Delta\tilde{\rho}_k^{INS} = -\left(\mathbf{n}_k(t_M), \Delta\tilde{\mathbf{R}}_{INS} + \Delta\tilde{\mathbf{C}}_b^N \cdot \mathbf{L}_{IMU}^{Laser}\right) \tag{15}$$

and, $\mathbf{L}_{IMU}^{Laser}$ is the IMU to laser scanner lever arm resolved in the body-frame. Note that equations (14) and (15) represent a specific implementation of the generic multi-sensor fusion observable defined by equation (1) for the case of laser/inertial data fusion.

GPS and laser observables of the Kalman filter are combined into a joint filter measurement vector:

$$\mathbf{y}_{Kalman} = \left[u_1^{Kalman} \quad \ldots \quad u_J^{Kalman} \quad v_1^{Kalman} \quad \ldots \quad v_K^{Kalman}\right]^T \tag{16}$$

As mentioned previously the Kalman filter implements the dynamic-state estimation approach: i.e., the filter does not estimate absolute position; instead, position changes between GPS and laser scanner measurement updates are estimated. The state vector for the dynamic-state filter formulation includes twenty states: delta position error states (three states); velocity error states (three states); attitude error states (three states); delta attitude error states (three states) - these are attitude errors accumulated over the filter update interval; gyro bias states (three states); accelerometer bias states (three states); and, GPS receiver clock states that include delta bias state and drift state. For this state vector, the filter observation matrix ($\mathbf{H}_{Kalman}$) is derived from the filter observation equations (9), (10), (14) and (15). Elements of this matrix projections of filter states into the filter observation domain as illustrated in Figure 8.

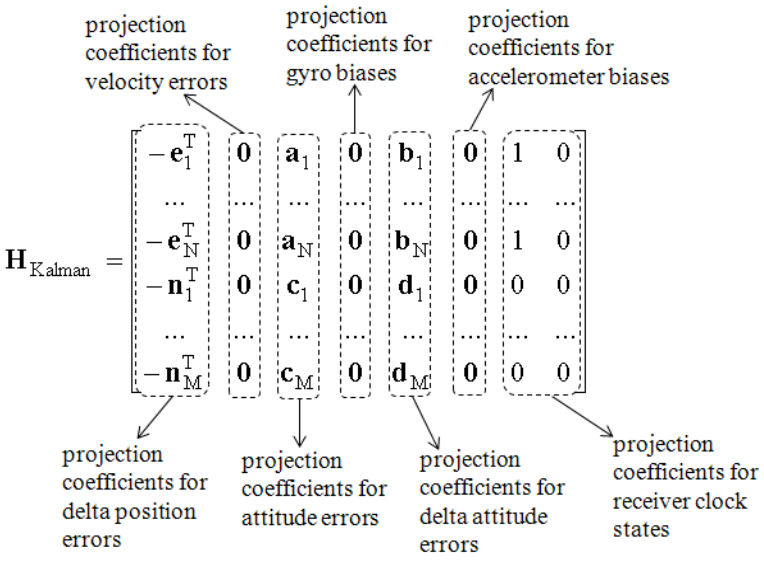

Figure 8: Kalman filter observation matrix: matrix elements define projection coefficients for projecting filter states into the filter observation domain.

In Figure 8:

0's are 3x1 zero rows;
and **a**, **b**, **c**, **d** are 3x1 rows that account for the transformation of INS attitude error terms into the filter observables through the lever-arm compensation.

These matrices were derived using the approach proposed in [17]. Results of the derivation are as follows:

$$\begin{aligned}
\mathbf{a}_j &= \left(\mathbf{e}_j \times \left(\Delta\tilde{\mathbf{C}}_b^N \cdot \mathbf{L}_{IMU}^{GPS}\right)\right)^T \\
\mathbf{b}_j &= \left(\mathbf{e}_j \times \left(\tilde{\mathbf{C}}_b^N(t_{M-1}) \cdot \mathbf{L}_{IMU}^{GPS}\right)\right)^T \\
\mathbf{c}_k &= \left(\mathbf{n}_k \times \left(\Delta\tilde{\mathbf{C}}_b^N \cdot \mathbf{L}_{IMU}^{Laser}\right)\right)^T \\
\mathbf{d}_k &= \left(\mathbf{n}_k \times \left(\tilde{\mathbf{C}}_b^N(t_{M-1}) \cdot \mathbf{L}_{IMU}^{Laser}\right)\right)^T
\end{aligned} \tag{17}$$

where:

$\times$ is the vector dot product.

The filter measurement noise matrix is a diagonal matrix defined by variances in carrier phase SDs and line delta ranges:

$$\mathbf{R}_{Kalman} = \text{diag}\left(\sigma^2_{\Delta\varphi_1},...,\sigma^2_{\Delta\varphi_J},\sigma^2_{\Delta\rho_1},...,\sigma^2_{\Delta\rho_K}\right) \tag{18}$$

Carrier phase sigmas ($\sigma_{\Delta\varphi_k}$) are computed as follows:

$$\begin{aligned}
&\sigma^2_{\Delta\varphi_j} = \sigma^2_{\varphi_j}(t_M) + \sigma^2_{\varphi_j}(t_{M-1}) \\
&\sigma_{\varphi_j}(t_M) = \frac{\lambda_{L1}}{2\pi} \cdot \sqrt{\frac{1}{T_{int}} \cdot 10^{-\frac{C/No_j(t_M)}{10}}} \\
&j = 1,...,J
\end{aligned} \tag{19}$$

where:

λ_{L1} is wavelength of the GPS link 1 (L1) carrier (0.19 cm, approximately);
T_{int} is the GPS receiver signal integration interval; and,
C/No is the carrier-to-noise ratio that is routinely estimated by the open loop GPS receiver.

Laser delta range sigmas ($\sigma_{\Delta\rho_k}$) are calculated based on equation (20):

$$\begin{aligned}
&\sigma^2_{\Delta\rho_k}(t_M) = \sigma^2_{\rho_k}(t_M) + \sigma^2_{\rho_k}(t_{M-1}) \\
&k = 1,...,K
\end{aligned} \tag{20}$$

where:

$\sigma_{\Delta\rho_k}$ are line range sigmas that are estimated using the approach reported in [20].

With the filter states listed above, filter measurements formulated by equations (9), (10), (14) and (15), and filter matrices represented in Figure 8 and defined by equations (17) and (18), the INS drift estimation procedure implements a complementary Kalman filter algorithm for the estimation of the inertial error states

and GPS receiver clock states. The filter formulation is similar to the GPS/INS Kalman filter model found in [16].

Performance of the GPS/laser scanner/inertial solution is illustrated below using experimental data collected in real urban environments. A test van was used as a platform for urban data acquisition. The data were acquired in Athens, Ohio, USA. Figure 9 shows a photograph of the data collection setup.

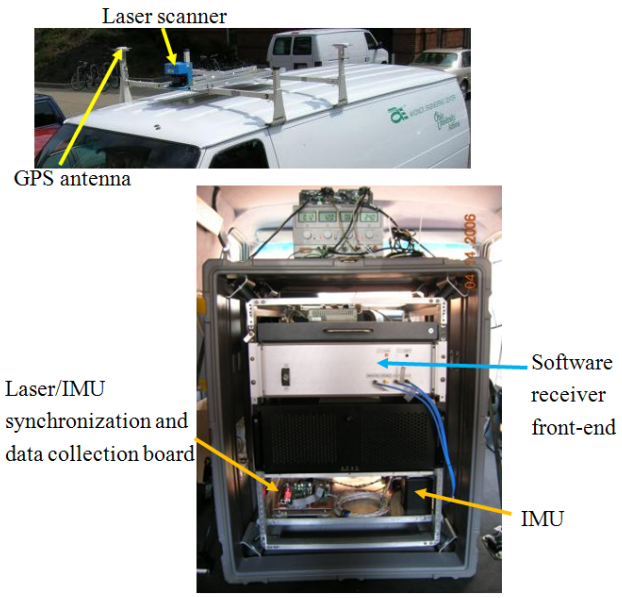

Figure 9: Data collection setup used for the acquisition of GPS/Laser scanner/inertial urban test data.

The setup used to acquire and process live GPS, laser scanner, and inertial urban data includes:

- Laser scanner: SICK LMS-200. A centimeter distance measurement mode was chosen. For this mode, a standard deviation of the laser ranging noise is specified as 5 mm. The maximum measurement range is 80 m. A scan angular range is from 0 to 180 deg with an angular resolution of 0.5 deg. A scanner update rate of one scan per 0.4 s was used.
- IMU: Systron Donner DQI IMU. This IMU represents a tactical-grade unit whose main characteristics are summarized in Table 1.
- GPS receivers: A software receiver front-end developed at the Ohio University Avionics Engineering Center was used for collection of raw GPS signal samples [21]. A NovAtel Superstar II receiver provided 1 PPS signal for time-stamping of laser scanner and inertial measurements.
- Synchronization and data collection board: Xilinx Spartan-3 Field Programmable Gate Arrays (FPGA). The board decodes laser and inertial data from corresponding measurement sensors, time stamps the measurements decoded using 1 PPS signal, and then sends time-stamped measurements via a Digilent USB board to a PC that collects the data for post-processing.
- Data processing: Post-processing implemented in Matlab™.

Table 1: IMU characteristics.

Parameter	Value
Gyro bias in-run stability	3 deg/hr (sigma)
Gyro noise	$0.035\ \text{deg}/\sqrt{\text{hr}}$ (sigma)
Gyro scale factor	350 ppm (sigma)
Accelerometer bias in-run stability	200 μg (sigma)
Accelerometer noise	$200\ \mu\text{g}/\sqrt{\text{Hz}}$ (sigma)
Accelerometer scale-factor	350 ppm (sigma)
Sensor axis non-orthogonality	0.5 mrad

Figure 10 shows test trajectory implemented for the first test scenario. This figure shows the vehicle trajectory along with images of the environment taken at select trajectory points. The test trajectory shown is reconstructed by the laser/INS integration that is described in [5].

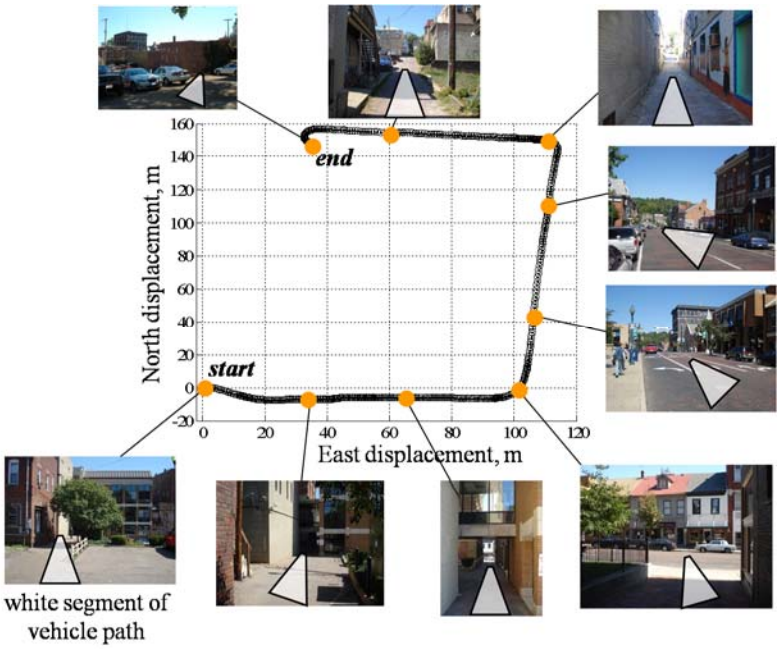

Figure 10: Test trajectory: trajectory reconstructed by the laser/INS integration is shown along with images of the environment taken at select trajectory points.

As it can be seen from the images represented, the test trajectory includes both relatively open streets as well as dense urban canyons. Thus, this trajectory allows testing performance of the integrated solution in a variety of urban environmental conditions.

Figure 11 illustrates complementary availability of GPS and laser measurements for the first test scenario. Availability of GPS measurements is represented by satellite tracking statuses. A particular satellite is designated by its pseudorandom code number (PRN). The satellite tracking status is shown using a black-to-white color scheme. Black color indicates satellites with a strong C/No (50 dB-Hz or higher). White color is used for satellites with a C/No value below the tracking threshold of 32 dB-Hz: i.e. white color indicates that a satellite is not visible. The black-to-white color scheme is also applied to illustrate the availability of features

extracted from scan images. Black color indicates that multiple lines are extracted from scan images and the line geometry allows for complete navigation computations. White color designates cases where no lines are extracted. As shown in Figure 11, GPS and laser scanner measurements exhibit complementary availability. Limited or no GPS measurements are available in dense canyons where multiple lines are extracted from scan images: see, for example, a portion of the plot that corresponds to the urban canyon image. Vice-versa, a sufficient number of visible satellites is present on open streets where limited or no lines are extracted from laser scans: see, for example, a portion of the plot that corresponds to the open street image.

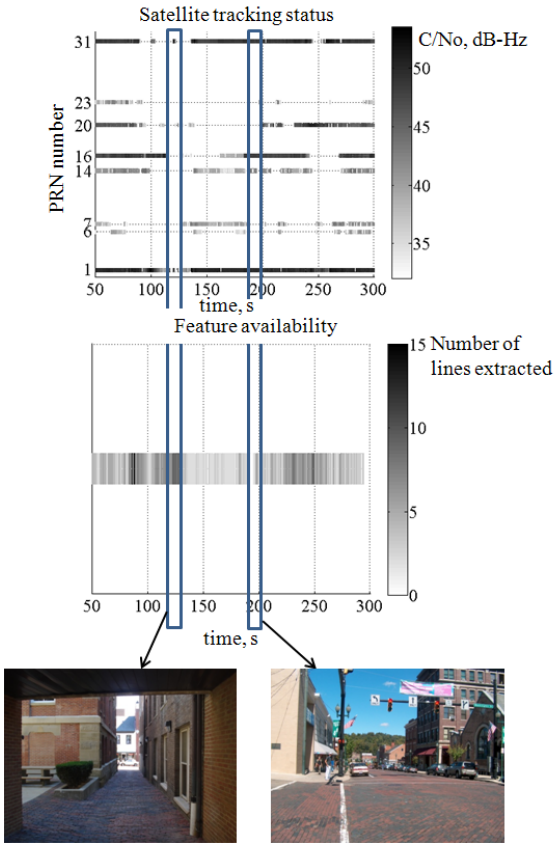

Figure 11: Complementary availability of GPS and laser scanner measurements.

Delta position residuals are applied to characterize the trajectory estimation performance. Residual vector ($\delta\mathbf{R}$) is computed as the difference between the laser/GPS weighted LMS estimate of the delta position ($\Delta\mathbf{R}_{\text{Laser/GPS}}$) and inertial delta position ($\Delta\mathbf{R}_{\text{INS}}$) that is compensated for drift terms using Kalman filter predictions:

$$\delta\mathbf{R} = \Delta\mathbf{R}_{\text{Laser/GPS}} - \Delta\mathbf{R}_{\text{INS}} - \left(\tilde{\mathbf{C}}_{\text{b}}^{\text{N}}(t_{\text{M}}) - \tilde{\mathbf{C}}_{\text{b}}^{\text{N}}(t_{\text{M-1}})\right)\cdot\mathbf{L}_{\text{IMU}}^{\text{GPS}} \tag{21}$$

The GPS/Laser LMS delta position solution is computed based on GPS carrier phase SDs and laser line delta ranges without the use of the inertial. LMS estimation details are given in [8]. Essentially, delta position residuals characterize the level of noise in the reconstructed trajectory. This noise is a combined effect of the

GPS carrier phase noise, noise in line ranges and the noise component of INS position drift. Figure 12 shows residual plots for East and North components of delta position.

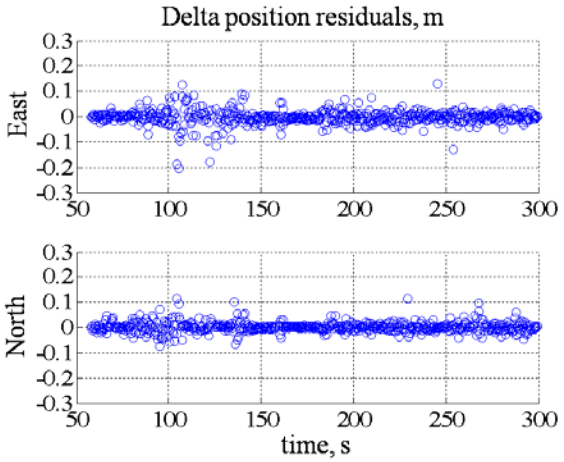

Figure 12: Delta position residuals for the GPS/laser/INS urban test example.

The standard deviations of East and North residual components are computed as 3.0 cm and 2.0 cm, respectively. For a similar test trajectory, residual standard deviations of the laser/INS integrated implementation (i.e., when GPS observables of the Kalman filter are not used) are at a 7-cm level [5]. GPS/ laser/INS residual noise is generally increased when the LMS solution relies primarily on line ranges as compared to cases with good satellite availability. This is due to a higher level of noise in line ranges (caused mostly by the texture of scanned urban surfaces) as compared to the carrier phase noise. For example, an increased residual noise can be observed for the time interval starting at approximately 60 s and ending at approximately 130 s. This interval corresponds to a part of the trajectory that belongs to dense urban environments where limited satellites are available: for illustration of the environment, see the third image from the trajectory start in Figure 10.

3.2 Vision/Laser Scanner/Inertial Integration

Vision-based navigation techniques serve as a viable option for autonomous, passive navigation and guidance in Global Positioning System (GPS)-denied environments [9]. However, vision-based methods, including stereo-vision, are known to be brittle to signal noise, particularly in terms of estimating the image depth. Stereo vision suffers from several disadvantages. The first is synchronization: if the stereo system is moving, and the two images are not captured at the same time, the time discrepancy between the two images can invalidate the stereo reconstruction. This timing discrepancy cannot be completely compensated using the relative motion information (provided, for example, by the inertial navigation) due to the unknown image depth. A second problem is "vergence," i.e. the fact that the area of interest must be in the field of view (FoV) of both cameras, and must be focused in both cameras. This typically requires different orientation of the cameras for close targets (e.g. more "cross-eyed") and far targets. Differences in the optical response of the two cameras can also make matching more difficult. Monocular vision methods give a scaled estimate of camera motion and a scaled estimate of scene structure. This scaled estimate is the major drawback of monocular methods, and requires additional sensors or information to recover the correct scale.

The fusion of vision and laser data is applied for efficient resolution of the scale ambiguity and performance enhancement of the navigation accuracy and reliability in the face of image noise. Laser scan data are

exploited to initialize three-dimensional (3D) tracking of stationary features and to enhance the feature tracking performance. Example 3D features include planar surfaces (characterized by range and normal vector) and point features (characterized by their Cartesian coordinates). Changes in feature parameters between images are used for navigation. Inertial data are applied to perform robust feature matching between images and coasting in environments where insufficient features are available. INS data can also be used to adjust laser scan range measurements for platform motion in order to compensate for the time discrepancy between camera images and laser scans. The proposed integration concept allows for the initialization of 3D feature tracking based on a limited number of laser scans: two scans are required, after which the system can operate in a completely passive mode. This serves as an important aspect for many surveillance, reconnaissance and navigation missions.

To improve the robustness of the navigation solution, the vision/laser integrated mechanization is augmented with inertial sensor measurements. INS outputs are exploited for robust matching of the features that are extracted from vision and laser data. The use of INS outputs for feature matching in video images is described in [9]. Details of the INS-based feature matching in laser scan images are discussed in [5]. Inertial data are also used to coast through those cases where a limited number of features is available. Figure 13 shows a high-level diagram of the Vision/Laser/INS integrated mechanization.

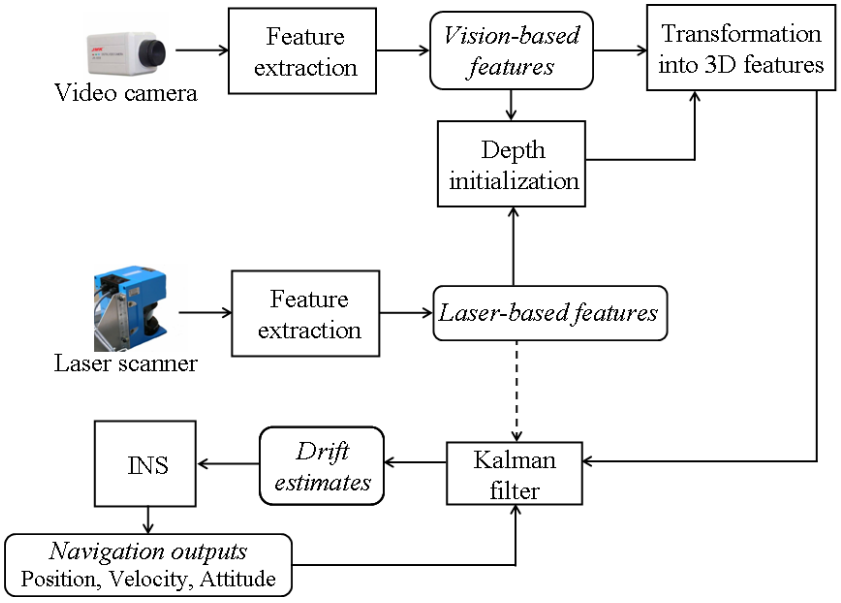

Figure 13: Vision/Laser/INS Integrated Solution.

Laser scanner measurements are used to initialize the depth estimate of the vision-based features. As stated previously, a very limited number of scans (two scans) is sufficient for the image depth initialization. Following the initialization step, the system can operate in a complete passive mode using vision-based features only. Navigation accuracy can be improved considerably if periodic scans at a limited rate (such as, for example, one scan per 30 s) are applied. This aspect is explained in more details in the feasibility demonstration discussion below. For those cases where the active component of the laser measurement mechanism does not represent a concern (i.e. for the majority of civil use cases), laser scanner can operate continuously to provide additional feature measurements in order to improve the navigation performance.

The vision/laser/INS mechanization shown in Figure 13 estimates the navigation solution (position, velocity, and attitude) from the INS. Vision and laser feature measurements are applied to estimate inertial error states in order to mitigate drift in inertial navigation outputs. Laser-based observables of the Kalman filter are defined by equations (12) through (15) above.

Equation (22) formulates vision-based observables of the Kalman filter using the unit sphere representation of image features that supports multi-aperture camera cases [22]:

$$\eta_p^{\text{Kalman}} = \begin{bmatrix} \left(\tilde{\mathbf{n}}_p^{(2)}\right)^T \cdot \Delta\tilde{\mathbf{C}}_N^b \cdot \mathbf{B} \cdot \Delta\tilde{\mathbf{R}}_{\text{INS}} - \left(\tilde{\mathbf{n}}_p^{(1)}\right)^T \cdot \mathbf{B}^T \cdot \Delta\tilde{\mathbf{C}}_b^N \cdot \tilde{\mathbf{n}}_p^{(2)} \cdot \hat{\rho}_p^{(1)} \\ \left(\tilde{\mathbf{n}}_p^{(2)}\right)^T \cdot \Delta\tilde{\mathbf{C}}_N^b \cdot \mathbf{D}_p \cdot \Delta\tilde{\mathbf{R}}_{\text{INS}} - \left(\tilde{\mathbf{n}}_p^{(2)}\right)^T \cdot \Delta\tilde{\mathbf{C}}_N^b \cdot \tilde{\mathbf{n}}_{\perp p}^{(1)} \cdot \hat{\rho}_p^{(1)} \end{bmatrix} \quad (22)$$

$$p = 1,...,P$$

where:

$\tilde{\mathbf{n}}_p^{(s)}$, $p = 1,..,P$, $s = 1,2$ is the unit vectors of the feature p (i.e. the unit vector pointed from the center of the camera to the feature p) that is extracted from image s;
$\tilde{\mathbf{n}}_{\perp p}^{(s)}$ is the unit vector that is perpendicular to the feature unit vector; $\hat{\rho}_p^{(1)}$ is the estimated feature range for image 1;
$\Delta\tilde{\mathbf{R}}_{\text{INS}}$ and $\Delta\tilde{\mathbf{C}}_b^N$ are INS position and orientation changes between images 1 and 2; and,
matrices B and D are defined as follows:

$$\mathbf{B} = \begin{bmatrix} 0 & -1 & 0 \\ 1 & 0 & 0 \\ 0 & 0 & 0 \end{bmatrix}, \quad \mathbf{D_p} = \begin{bmatrix} 0 & 0 & -\cos(\varphi_p^{(1)}) \\ 0 & 0 & -\sin(\varphi_p^{(1)}) \\ \cos(\varphi_p^{(1)}) & \sin(\varphi_p^{(1)}) & 0 \end{bmatrix} \quad (23)$$

where:

$\varphi_p^{(1)}$ is the feature spherical azimuth angle as measured from image 1.

Image 1 is generally the image where the feature was first observed and image 2 is the current image. Equation (22) is linearized to support the linear formulation of the complementary Kalman filter.

As stated previously the key motivation for combining vision and laser data is the use of laser scan measurements for the estimation of the unknown depth of video images. The estimation approach is illustrated in Figure 14.

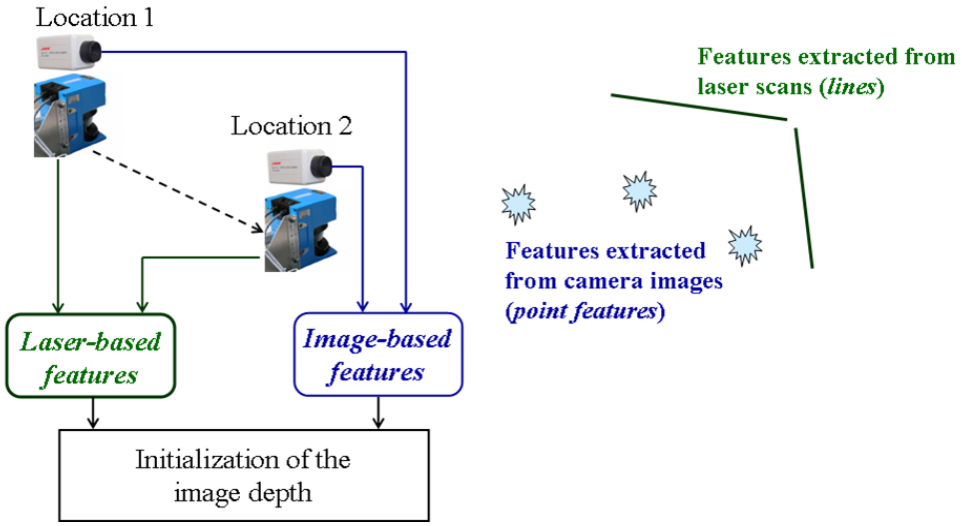

Figure 14: Image depth initialization method.

The depth estimation exploits two images from a video camera and two laser scan images that are acquired at two different locations. It is assumed that the camera and the laser are mounted on the same platform and their measurement frames are collocated. Parameters of features that are extracted from laser scan images and video images at two locations of the platform are used to estimate the image depth. The estimation does not require the camera and the laser to observe the same features: i.e., video and laser features can be completely unrelated to each other. The initialization method discussed in this paper assumes that point features are extracted from video images and lines are extracted from laser scans. This method can be generalized to include other types of features.

To provide a conceptual illustration of the depth initialization method, a simplified 2D case is considered below. This case is illustrated in Figure 15.

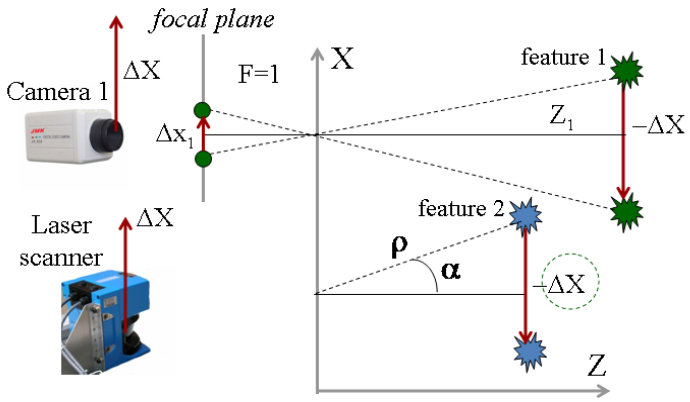

Figure 15: Illustration of the depth initialization method: simplified 2D case.

Camera and laser are placed on the same moving platform and their measurement frames are aligned. The platform moves along the X axis of the XZ navigation coordinate frame. The camera optical axis is aligned

with the Z axis of the frame. For simplicity, it is assumed that the camera focal length F equals unity. Feature 1 is observed by the camera and feature 2 is observed by the laser scanner. As stated previously, these features may be completely unrelated. The platform displacement ΔX transforms into the displacement of the vision-based feature as:

$$\Delta x^{(1)} = \Delta X / Z^{(1)} \tag{24}$$

where:

$Z^{(1)}$ is the unknown depth.

The laser scanner observes feature 2. The distance to this feature is directly measured by the scanner: 2D scan points are generally represented by their polar coordinates that include range and polar angle. Polar coordinates of feature 2 that are extracted from two scan images are applied to estimate the platform displacement:

$$\Delta\hat{X} = -\left(\rho_2^{(2)} \sin(\alpha_2^{(2)}) - \rho_1^{(2)} \sin(\alpha_1^{(2)})\right) \tag{25}$$

where:

$\left(\rho_1^{(2)}, \alpha_1^{(2)}\right)$ and $\left(\rho_2^{(2)}, \alpha_2^{(2)}\right)$ are the range and polar angles of feature 2 in the first and second scan images, accordingly.

Platform displacement that is estimated based on scan data is then used to initialize the depth of the image-based feature:

$$\hat{Z}^{(1)} = \Delta\hat{X} / \Delta x^{(1)} \tag{26}$$

A similar approach is applied to estimate the image depth for a general 3D case. Equation (27) relates 3D Cartesian feature coordinates $\mathbf{M}_p$ to its homogeneous coordinates $\mathbf{m}_p$ in the 2D image frame:

$$\begin{aligned} \mathbf{M}_p^{(1)} &= Z_p^{(1)} \mathbf{m}_p^{(1)} \\ \mathbf{M}_p^{(2)} &= Z_p^{(2)} \mathbf{m}_p^{(2)} \\ p &= 1,\ldots,P \end{aligned} \tag{27}$$

where:

$Z_k^{(j)}$ is the depth of the k^{th} feature in the j^{th} image.

Cartesian feature coordinates in two images are related through the orientation change matrix and the translational vector:

$$\mathbf{M}_p^{(2)} = \Delta\mathbf{C}_b^N \left(\mathbf{M}_p^{(1)} - \Delta\mathbf{R}\right) \tag{28}$$

Substituting equation (27) into (28) then yields:

$$\mathbf{M}_p^{(2)} = \Delta\mathbf{C}_b^N \left(Z_p^{(1)} \cdot \mathbf{m}_p^{(1)} - \Delta\mathbf{R}\right) \tag{29}$$

Assuming that the optical axis is aligned with the Z- axis of the camera frame, the depth of the feature is related to its Cartesian coordinates as follows:

$$Z_p^{(j)} = \mathbf{n}_Z^T \cdot \mathbf{M}_p^{(j)} \tag{30}$$

where:

$\mathbf{n}_Z = \begin{bmatrix} 0 & 0 & 1 \end{bmatrix}^T$.

From equations (27) through (30), the following relationship can be derived [23]:

$$\begin{aligned} &\mathbf{H}_p \cdot \begin{bmatrix} \Delta\mathbf{R} \\ Z_p^{(1)} \end{bmatrix} = \mathbf{0}_{2\times 1} \\ &\mathbf{H}_p = \mathbf{A} \cdot \left(\mathbf{I}_{3x3} - \Delta\mathbf{C}_b^N \cdot \mathbf{m}_k^{(2)} \cdot \left(\mathbf{n}_Z^T \Delta\mathbf{C}_N^b \right) \right) \begin{bmatrix} \mathbf{I}_{3x3} & -\mathbf{m}_p^{(1)} \end{bmatrix} \\ &p = 1,\ldots,P \end{aligned} \tag{31}$$

where:

$\mathbf{A} = \begin{bmatrix} 1 & 0 & 0 \\ 0 & 1 & 0 \end{bmatrix}$;

$\mathbf{I}_{3x3}$ is the 3-by-3 unit matrix; and,

$\mathbf{0}_{2x1}$ is a 2x1 zero column.

Equation (31) formulates vision-based linear equations for the estimation of the image depth. Note that unknowns include the depth components ($Z_p^{(1)}$, p=1,…,P) and the displacement vector $\Delta\mathbf{R}$. The orientation change matrix is computed from the inertial data and is not estimated based on the laser/vision fusion. This allows for the linear formulation of the depth estimation problem. Note that in this case a correlation between inertial angular errors and initial depth estimates is created. This correlation must be taken into account in the design of the Kalman filter that estimates inertial drift states.

The solution of the equation system (31) is not unique. The displacement vector and depth can only be determined within an ambiguity of a scale-factor γ: i.e., if $\Delta\hat{\mathbf{R}}$ and $\hat{Z}_p^{(1)}$ satisfy the system (31), then $\gamma\Delta\hat{\mathbf{R}}$ and $\gamma\hat{Z}_p^{(1)}$ satisfy this system as well. To remove the scale-factor ambiguity, the system (31) is augmented by laser measurement observables. Line features are extracted from laser images and applied for the image depth initialization. It is assumed herein that lines are created in 2D scan images as a result of the intersection of the horizontal laser scanning plane with vertical planes (such as building walls in urban environments). In this case, the relationship between changes in line parameters and displacement vector components is formulated by equation (11) above, which, in the matrix form, is expressed as follows:

$$\begin{aligned} &\mathbf{n}_k^T \Delta\mathbf{R} = \rho_k^{(1)} - \rho_k^{(2)} \\ &\mathbf{n}_k = \begin{bmatrix} \cos(\alpha_k^{(1)}) & \sin(\alpha_k^{(1)}) \end{bmatrix}^T \\ &k = 1,\ldots,K \end{aligned} \tag{32}$$

Equation (32) provides the laser part of the mage depth estimation relations. Combining (32) with the vision-based part defined by equation (31) yields:

$$\mathbf{H}_p \cdot \begin{bmatrix} \Delta\mathbf{R} \\ Z_p^{(1)} \end{bmatrix} = \mathbf{0}_{2\times 1}, p = 1,...,P$$
$$\mathbf{n}_k^T \Delta\mathbf{R} = \rho_k^{(1)} - \rho_k^{(2)}, k = 1,...,K \quad (33)$$

Equation (33) defines a linear system of equations for the estimation of image depth. Note that the minimum feature configuration that is required to initialize the image depth based on equation (33) includes three vision features and one laser feature. In this case, seven equations are available (two per vision feature and one for the laser feature) to estimate six unknowns (three depth values and three components of the displacement vector).

The image depth initialization method was verified with experimental data. Indoor experimental data were collected in hallways of the Air Force Research Laboratory at Eglin Air Force Base. Figure 16 shows a photograph of the data collection setup.

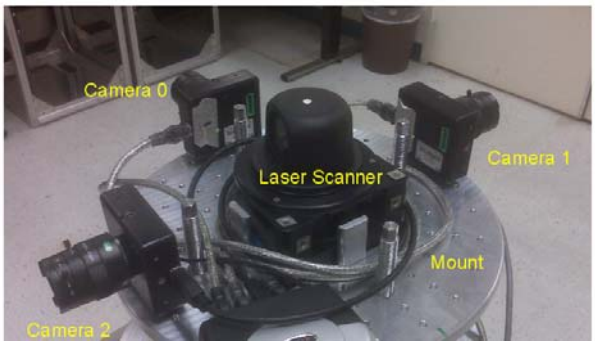

Figure 16: Data collection setup used for demonstrating the feasibility of the laser/vision depth estimation.

The data collection setup includes a laser scanner and three video cameras. This setup was assembled for the development and verification of the laser scanner/multi-aperture video data fusion. Only one video camera was used for the experiment discussed herein. A straight motion trajectory was implemented. Two laser scans were used to initialize the depth of video images. Following the depth initialization, the displacement vector was estimated based on vision features only without the use of laser scan data. Vision-based displacement estimates were compared to the reference motion trajectory. To construct the reference trajectory, cm-accurate displacement information was estimated from laser scan images as described in reference [5]. Figure 17 exemplifies experimental results.

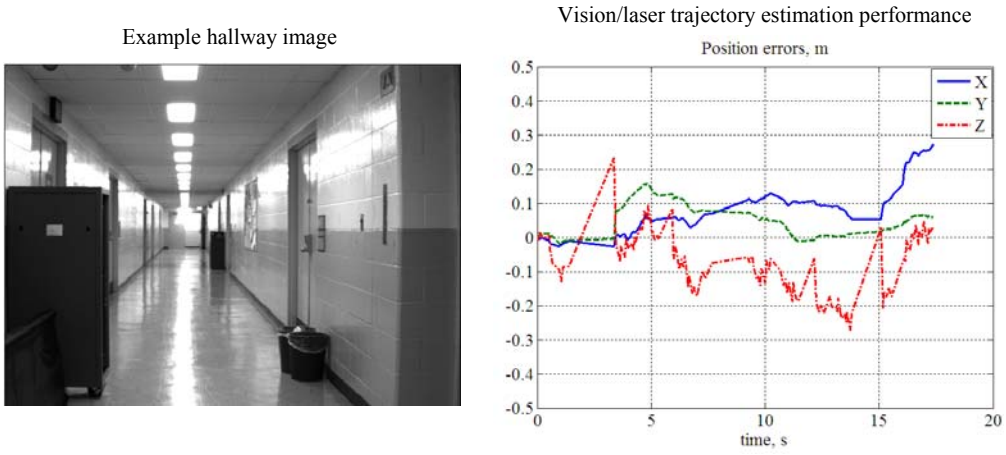

Figure 17: Example of the vision/laser trajectory estimation performance: only two laser scans are applied to initialize the image depth (at the system start-up and at about 5 seconds after the beginning of the experiment); following the depth initialization, 3D position components are estimated based on video images only.

Experimental data presented show that decimeter-level positioning accuracy that is achieved using video images and two laser scans to initialize the image depth. These results clearly demonstrate the feasibility of the semi-passive navigation approach that uses very limited laser scans (two scans for the example case considered herein) for the initialization of 3D image-based navigation.

Feasibility of the vision/laser/INS mechanization described above was assessed in an indoor simulated environment that was implemented in Matlab. For the simulation, the sensor specifications were implemented as follows:

- Video: a multi-aperture camera head that includes three video cameras (see Figure 16 for the illustration of the multi-aperture implementation); the angular separation between the camera optical axis is 120 deg; for each camera the resolution is 640x480, the azimuth FoV is 40 deg, the elevation FoV is 40 deg, and, the update rate is 10 Hz;
- Laser scanner: measurement range is 80 m; angular range: is from 0 to 360 deg; range noise is 1 cm (std); and, angular resolution is 0.5 deg;
- Inertial measurement unit: accelerometer bias is 1 mg; and, gyro drift is 50 deg/hr.

Figure 18 illustrates a 2D horizontal projection of the simulated indoor environment that includes multiple indoor hallways. Hallway walls were simulated as vertical with the wall height equal to 2.5 m. A horizontal motion trajectory with the absolute velocity value of 1 m/s was implemented as shown in Figure 18.

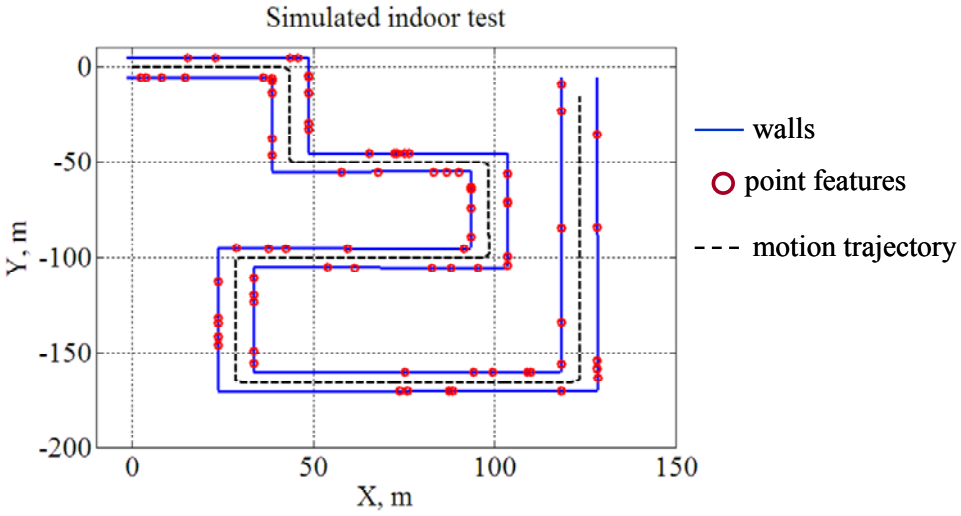

Figure 18: Simulated indoor environments.

Figure 19 shows performance of the vision/inertial integration, i.e., the use of laser measurements.

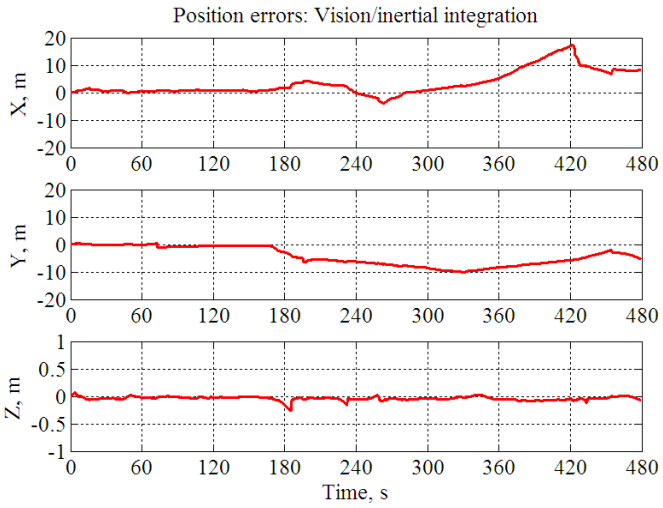

Figure 19: Performance of the vision/inertial integration for the indoor simulated environment.

In this case, the feature depth is initialized by observing the feature from two different location of the platform and using inertial displacement and orientation change measurements for the unambiguous estimation of the image depth as described in [22]. Simulation results shown in Figure 19 indicate that position errors of the vision/INS integration stay in the range from -10 m to 20 m. This level of navigation performance is improved significantly if laser scanner measurements are incorporated into the solution. Figure 20 illustrates performance of the vision/laser/INS mechanization for the case where a 1-s update rate of laser images is used.

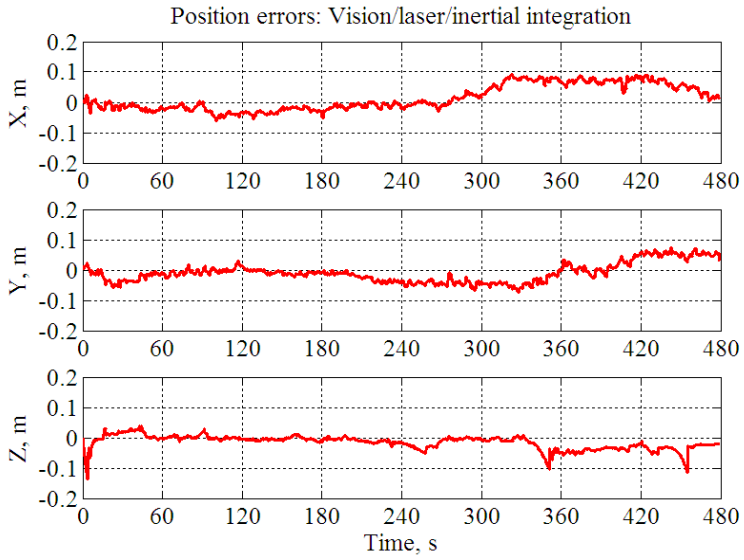

Figure 20: Performance of the vision/inertial integration for the indoor simulated environment: 1-s laser updates.

The use of a 1-s laser updates enables cm-accurate estimation of the 3D position vector. Figure 21 shows simulation results for the case where periodic laser scans at a very limited rate are applied. In this case, laser scans are made only once per 30 s.

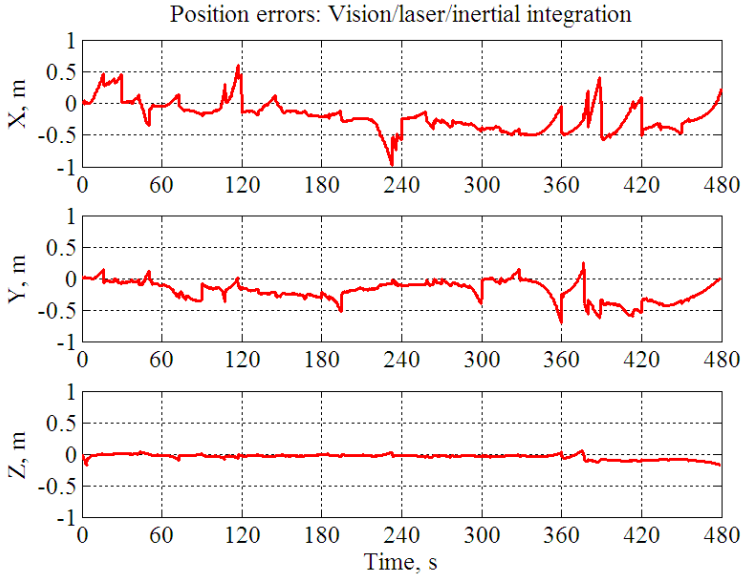

Figure 21: Performance of the vision/inertial integration for the indoor simulated environment: 30-s laser updates.

It is important to note that the system that employs laser scans at this low rate can be still considered as practically passive since, from the practical point of view, a laser scanning at this rate cannot be detected.

Positioning accuracy is maintained at a sub-m-level, which provides an order of magnitude performance improvement as compared to the vision/laser implementation. Therefore, for the vision/laser/INS integration it is extremely beneficial to use the system implementation that operates in a semi-passive mode employing periodic scans at a limited scan rate.

4.0 SUMMARY

Navigating in difficult environments requires the use of multi-sensor fusion techniques. This paper proposes a generic multi-sensor fusion approach and applies this approach for developing GPS/laser scanner/inertial and vision/laser/inertial integrated mechanizations. Simulated data and data collected in various urban indoor and outdoor environments show that multi-sensor fusion techniques developed demonstrate a significant potential for enabling reliable and accurate navigation capabilities for a variety of challenging navigation scenarios.

DISCLAIMER

The views expressed in this article are those of the authors and do not reflect the official policy or position of the United States Air Force, Department of Defense, or the U.S Government.

REFERENCES

[1] Titterton, D. H., and Weston J. L. *Strapdown Inertial Navigation Technology*, Second Edition, The American Institute of Aeronautics and Astronautics, Reston, Virginia, USA and The Institute of Electrical Engineers, Stevenage, UK, 2004

[2] A. Soloviev, S. Gunawardena, F. van Graas, "Deeply Integrated GPS/Low-Cost IMU for Low CNR Signal Processing: Concept Description and In-Flight Demonstration" NAVIGATION, Journal of the Institute of Navigation, Vol. 54, No. 1, 2008

[3] E. Kaplan and C. Hegarty (Editors), *Understanding GPS: Principles and Applications*, 2nd ed. Norwood Massachusetts, USA: Artech House, 2006

[4] F. Van Graas, A. Soloviev, M. Uijt de Haag, and S. Gunawardena, "Closed-Loop Sequential Signal Processing and Open-Loop Batch Processing Approaches for GNSS Receiver Design," *IEEE Journal on Selected Topics in Signal Processing*, Vol. 3, Issue 4, August 2009.

[5] A. Soloviev, D. Bates, and F. van Graas, "Tight Coupling of Laser Scanner and Inertial Measurements for a Fully Autonomous Relative Navigation Solution," *NAVIGATION, Journal of the Institute of Navigation*, Vol. 54, No. 3, Fall 2007.

[6] G.T. Schmidt, R.E. Phillips, "INS/GPS Integration Architectures," NATO RTO Lecture Series, Spring 2010.

[7] A. Soloviev, D. Bruckner, F. van Graas, and L. Marti, "Assessment of GPS Signal Quality in Urban Environments Using Deeply Integrated GPS/IMU," in *Proceedings of the Institute of Navigation National Technical Meeting*, January 2007

[8] A. Soloviev, "Tight Coupling of GPS, Laser Scanner, and Inertial Measurements for Navigation in Urban Environments," in *Proceedings of IEEE/ION Position Location and Navigation Symposium*, May 2008.

[9] Veth, M. and J. Raquet, "Fusion of Low-Cost Imaging and Inertial Sensors for Navigation," *Proceedings on ION GNSS-2006*, September 2006.

[10] Barnes, J., C. Rizos, M. Kanli, D. Small, G. Voigt, N. Gambale, J. Lamance, T. Nunan, C. Reid, "Indoor Industrial Machine Guidance Using Locata: A Pilot Study at BlueScope Steel," *Proceedings of 2004 ION Annual Meeting*, June 2004.

[11] Opshaug, G. and P. Enge, "GPS and UWB for Indoor Positioning," *Proceedings of ION GPS-2001*, September 2001.

[12] Rabinowitz, M. and J. Spilker, "The Rosum Television Positioning Technology," *Proceedings of 2003 ION Annual Meeting*, Albuquerque, June 2003.

[13] Eggert, R. and J. Raquet, "Evaluating the Navigation Potential of the NTSC Analog Television Broadcast Signal," *Proceedings of ION GNSS-2004*, September 2004.

[14] Hall, T, C. Counselman III, P. Misra, "Radiolocation Using AM Broadcast Signals: Positioning Performance," *Proceedings of ION GPS-2002*, September 2002.

[15] McEllroy, J., J. Raquet, and M. Temple, "Use of a Software Radio to Evaluate Signals of Opportunity for Navigation," *Proceedings on ION GNSS-2006*, September 2006.

[16] R. G. Brown and P. Y. C. Hwang, *Introduction to Random Signals and Applied Kalman Filtering*, 3rd ed., John Wiley & Sons, Inc., New York, 1997.

[17] J. L. Farrell, "GPS/INS-Streamlined," *NAVIGATION, Journal of the Institute of Navigation*, Vol. 49, No. 4, Summer 2002.

[18] F. van Graas and A. Soloviev "Precise Velocity Estimation Using a Stand-Alone GPS Receiver," *NAVIGATION, Journal of the Institute of Navigation*, Vol. 51 No. 4, 2004.

[19] D. Bates, "Navigation Using Optical Tracking of Objects at Unknown Locations," M.S. Thesis, Ohio University, 2006.

[20] D. Bates and F. van Graas "Covariance Analysis Considering the Propagation of Laser Scanning Errors use in LADAR Navigation," in *Proceedings of the Institute of Navigation Annual Meeting*, April 2007.

[21] S. Gunawardena, "Development of a Transform-Domain Instrumentation Global Positioning System Receiver for Signal Quality and Anomalous event Monitoring," Ph.D. Dissertation, Ohio University, June 2007.

[22] M. Miller, A. Soloviev, "Navigation in GPS Denied Environments: Feature-Based Navigation Techniques", NATO RTO Lecture Series, Spring 2010.

[23] A. Soloviev, N. Gans, M. Uijt de Haag "Integration of Video Camera with 2D Laser Scanner for 3D Navigation" in *Proceedings of the Institute of Navigation International Technical Meeting*, Jan 2009.